Bulletin of the Seismological Society of America, Vol. 70, No. 5, pp. 1715–1736, October 1980

FAULTING PROCESS OF THE MAY 17, 1976 GAZLI, USSR EARTHQUAKE

By Stephen Hartzell

ABSTRACT

The May 17, 1976 Gazli earthquake (m_b = 6.2, M_S = 7.0) has both seismological and engineering importance. Waveform modeling of long-period IDA Rayleigh waves, and WWSSN long- and short-period body waves indicates a thrust mechanism with strike N40°E, dip 54°SE, and rake of 78°. The moment is estimated to be 1.6 × 10^{26} dyne-cm; the fault area, 150 km^2; the average dislocation, 3.3 meters; and the average stress drop, 200 bars. Strong directivity effects due to a propagating rupture are present in both the long- and short-period teleseismic *P* waves. The data are not adequately explained by a simple point source, and require a three-dimensional, finite-source model. The relative amplitudes of *P* and *pP* at both long and short periods are used to deduce that the rupture started at a depth of 15 km and propagated almost entirely unilaterally upward, with an average rupture velocity of 2.0 to 2.5 km/sec. Simultaneous deconvolution of long- and short-period *P* waves reveals a complex, azimuthally dependent, source-time function. Finite-source models further suggest that a major part of the faulting was concentrated at depth, below 7 km. The strong-ground motion within 10 km of the fault is characterized by unusually high-amplitude (1300 cm/sec^2), high-frequency (10 Hz) accelerations and low-amplitude (10 cm), low-frequency (0.8 Hz) displacements. Synthetic Wood-Anderson records computed from the accelerograms give a local magnitude, M_L, of 6.35. The duration and character of the strong-ground motion is consistent with a rupture propagating upward in the general direction of the station.

Introduction

On April 8 and May 17, 1976, a pair of destructive earthquakes occurred in the Kyzylkum Desert in Uzbekistan, USSR, near the small settlement of Gazli. Gazli is located about 90 km northwest of the city of Bukhara, near the border of the USSR with Afghanistan (see Figure 1). The location and origin time of the April 8 event are reported to be 40.31°N 63.72°E at 02h 40m 23.9s and for the May 17 event, 40.35°N 63.45°E at 02h 58m 41.1s [*Bulletin of the International Seismological Centre* (ISC)]. The corresponding ISC depths are 10 and 14 km, respectively. Both events are given a body-wave magnitude of 6.2 (ISC), and a surface-wave magnitude of 7.0 [National Earthquake Information Service (NEIS)]. As a result of these two main shocks, all the structures in the town of Gazli were destroyed or rendered unsafe. At least 100 aftershocks were locally recorded from April 10 to May 16, some of them with felt intensities up to VI on the MSK scale. (The MSK scale is a Soviet intensity scale similar to Modified Mercalli.) Since 1976, there has been at least one other significant earthquake in the Gazli area: on June 4, 1978 at 19h 30m 23.4s, m_b = 6.0 (PDE).

In this paper, teleseismic waveforms are modeled over a wide range of periods to investigate the faulting process of the May 17, 1976 Gazli earthquake. The May 17 event is singled out because of an interesting, three-component accelerogram recorded at Karakyr Point, in the epicentral region. The Karakyr Point instrument was installed a few days after the April 8 earthquake by the Institute of the Physics of the Earth (USSR Academy of Sciences, Moscow). The Karakyr Point record is

one of the few existing recordings of strong ground motion within 10 km of a moderately large earthquake. Insight into understanding this important record is obtained through the study of the teleseismic waveforms.

Although this paper deals with a specific earthquake, three aspects of the work reported here appear to have general importance. First, this study points out the dangers of using a limited data set to estimate the focal mechanism of a dip-slip type earthquake. Without optimum station coverage, one nodal plane is usually poorly constrained, even when *SH* phases are included. Thus, it is often helpful, if not necessary, to consider surface-wave amplitudes. Second, the May 17 Gazli earthquake exhibits strong vertical directivity, as reflected in the amplitudes of teleseismic *P* and *pP* phases. Directivity, due to a propagation rupture, may be present in other moderately large earthquakes with dip-slip mechanisms. Thus, one should properly consider finite-source models for these events. Third, study of WWSSN short-period records for the Gazli earthquake illustrates the large amount of information which these records contain. The present study and other recent work (Ebel, 1979; Langston, 1978) show a surprising amount of correlation between certain WWSSN short-period stations. Observations such as these offer hope that short-period data can be utilized to resolve finer scale faulting details.

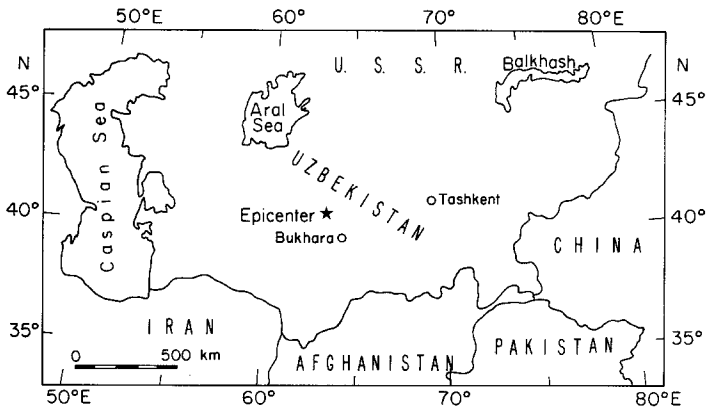

FIG. 1. Area map showing the location of the April 8 and May 17, 1976 Gazli earthquakes.

DATA ANALYSIS

Long-period body waves. All available WWSSN 70-mm microfilm records were examined for clear *P* and *S* phases, within the distance range of 30° to 90°. This distance window avoids upper mantle triplications and core shadow effects. Vertical *P* waves and both horizontal components of *S* waves, which could be accurately followed on the film record, were digitized and interpolated to a uniform time step of 0.25 sec. Waveforms were also corrected for the inherent skewness in the WWSSN recording system. The above screening process yielded 13 *P* waves and 11 pairs of *S* waves. Several additional records at stations closer than 30°, although off scale, furnished first motion information which was also used to constrain the mechanism. The *S* waves were then rotated to the back azimuth direction, using the ISC location, to obtain radial and tangential displacement.

Theoretical displacements are computed for a point shear dislocation in a layered half-space using generalized ray theory (Helmberger, 1974; Langston and Helmberger, 1975) and compared with the data. Attenuation is included by convolving the displacements with the causal Futterman (1962) Q operator with constant $t^* = T/Q$ (Carpenter, 1966). T is the ray travel time and Q is the average seismic quality factor

along the ray path. The t^* values of 1 and 4 are used throughout this paper for P and S waves, respectively. All source mechanism angles follow the convention of Langston and Helmberger (1975).

The source structure used in the calculation of the teleseismic synthetics is shown in Table 1. The model is based in part on two Soviet deep seismic-sounding profiles (Davydova *et al.*, 1975) and on a brief Soviet description of the local geology (Pletnev *et al.*, 1977). The two DSS profiles have a combined length of 230 km and run generally NNE by SSW, 50 to the southeast of Gazli. The profiles show a clear moho reflection at 41 km and a surface sedimentary layer of variable thickness. Pletnev *et al.* (1977) report 1420-meter thick sediments consisting of clays and sandstones underlain by highly resistant metamorphic schist. Although the model in Table 1 is rather detailed, the free surface is by far the most important interface in terms of teleseismically observed phases. Because of the dip-slip mechanism of the Gazli earthquakes, pP is the dominant reflected phase from the free surface. sP is larger for strike-slip mechanisms. [See Langston and Helmberger (1975) for examples.] When a surface sedimentary layer is present, reflected phases from the base of the sediments and P- to SV-converted phases within the sediments can also be important. The relative contributions of these phases will be illustrated in a later section. At this point, we could simply state the preferred fault plane solution and show the final comparisons between the data and synthetics. However, this approach

TABLE 1

LOCAL GAZLI STRUCTURE

Layer	α (km/sec)	β (km/sec)	ρ (gm/cm^3)	h (km)	D (km)
1	2.5	1.44	2.10	1.4	1.4
2	5.9	3.41	2.70	10.6	12.0
3	6.1	3.52	2.80	13.0	25.0
4	6.3	3.64	2.85	10.0	35.0
5	6.4	3.69	2.90	6.0	41.0
6	8.0	4.62	3.40	—	—

would not be very informative. Instead, a more detailed account will be given of how the focal mechanism was obtained. During the development, the importance of considering surface-wave data and more realistic finite-source models, will be stressed.

Figures 2 and 3 show observed (heavy traces) and synthetic waveforms for a proposed mechanism: strike N40°E, dip 54°SE, and rake 47°. This mechanism was obtained by a trial-and-error procedure of comparing synthetics with the data and is considered to give a good over-all fit to P and SH phases. However, the above mechanism is not the final preferred solution. A more detailed investigation points out the problems with the above mechanisms, as well as the simple source model used to generate it. The synthetics in Figure 2 and 3 are for a single-point shear dislocation at a depth of 15 km in the layered half-space of Table 1. The depth of 15 km is supported by short-period waveform modeling to be discussed later. A trapezoidal source-time function is assumed with a rise of 2 sec, top of 1 sec, and fall of 5 sec. The exact dimensions of the trapezoid are not particularly meaningful and can be changed by ±1 sec without greatly altering the synthetics. However, the longer decay time compared to the rise time appears to be a requirement of any model that fits the data. A sharp onset and a more gradual decay is also a property of theoretical dislocation time functions, such as the Kostrov (1964) model. The P-wave synthetics in Figure 2 represent the sum of the responses of eight generalized

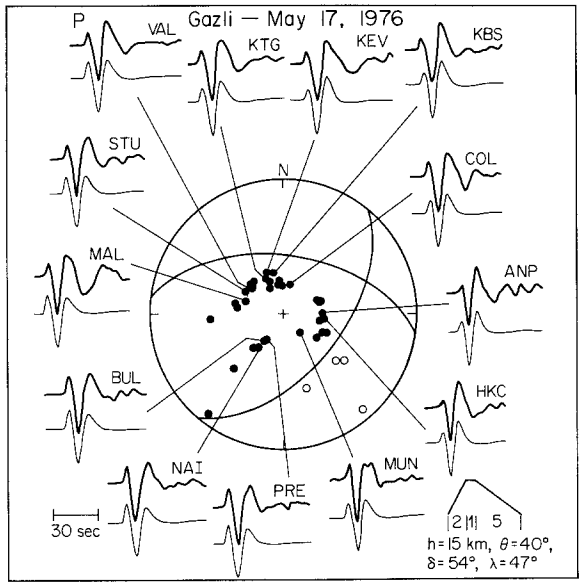

FIG. 2. Teleseismic *P* waves for an early model, which appears to explain the body-wave data, but not the surface-wave data. Observations are the top, heavy traces. Focal sphere is lower hemisphere projection.

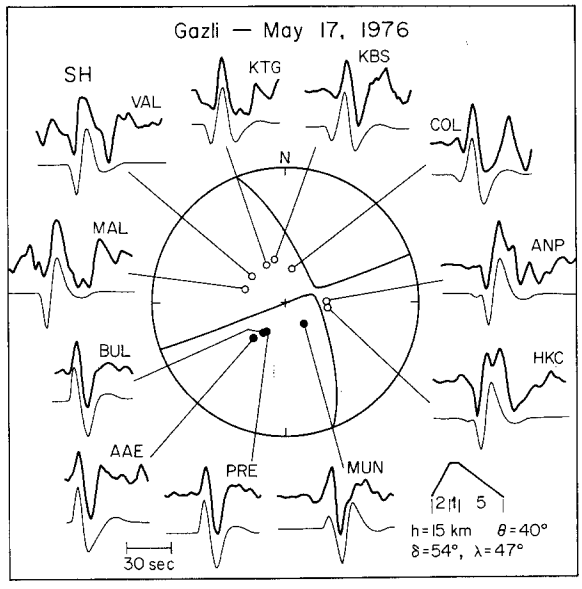

FIG. 3. Teleseismic *SH* waves for the same model as in Figure 2, which appears to explain the body-wave data, but not the surface-wave data. Observations are the top, heavy traces. Focal sphere is lower hemisphere.

rays: direct *P*, *pP*, and *sP* from the free surface, *pP* and *sP* from the base of the sediments (layer 1, Table 1), and the three most significant *P*- to *SV*-converted phases within the sedimentary layer. The *SH* synthetics in Figure 3 are the sum of three generalized rays: direct *S*, *sS* from the free surface, and *sS* from the base of the sediments.

The nodal plane dipping to the SE in Figure 2 is loosely constrained by first motions. However, there is very little constraint on the position of the second nodal

plane, which controls the rake of the fault. Although there is generally a good fit between the data and the synthetics, the *P*-wave synthetics are insensitive to the position of the EW-striking nodal plane. The standard procedure, in cases such as this, is to turn to *SH* waves to supply additional constraints. The *SH* synthetics in Figure 3 also appear to fit the data well, with the possible exceptions of stations HKC and ANP. At these two stations, there is a double pulse interference pattern in the latter half of the waveforms, which is not explained by the synthetics. It is tempting to write off this disagreement as being due to crustal, *S*-coupled *PL*-wave contamination. Longer period *PL* waves are probably present, following direct *S*, at COL and MAL. Thus, we have arrived at a mechanism which, with some liberty in interpretation of the data, is able to explain the observed body waveforms. However, as we will see in the following section, the above mechanism does not fit the surface-wave amplitudes. Herein lies the danger of considering a limited data set. The *P* and *SH* data, although fairly well distributed azimuthally around the focal sphere, are not sufficient to readily pick a specific mechanism with a high degree of confidence.

Surface-wave analysis. Surface waves are used to constrain the focal mechanisms by two approaches: (1) an inversion of R1 and R2 (Rayleigh waves) amplitude and phase data from the Project IDA network; and (2) a comparison between observed and theoretical R1 to G1 (Love waves) amplitude ratios at WWSSN stations. The IDA network is an array of digitally recording gravimeters (Agnew *et al.*, 1976) with excellent long-period response and calibration. Kanamori (in preparation) has developed an IDA inversion scheme, which uses Rayleigh wave amplitude and phase information at a specified period to invert for the focal mechanism and moment. At the time of the May 17, 1976 Gazli earthquake, two IDA stations were operating: NNA (Ñaña, Peru) and SUR (Sutherland, South Africa). Unfortunately, two stations are not sufficient to perform an accurate general inversion, with no external constraints on the focal mechanism. However, we have some constraint over one of the nodal planes from the preceding body-wave analysis. From Figure 2, a strike of N40°E and dip of 54°SE are used as fixed external constraints in the inversion. The inversion also assumes the spherically symmetric earth model and attenuation described by Kanamori (in preparation). The rake and moment are then computed using the amplitude and phase of R1 and R2 at NNA and SUR at periods of 256 and 197 sec. The periods are chosen long enough to reduce the effects of lateral heterogeneities, source complications, and at points in the spectrum where the signal-to-noise ratio is high. Inversion results at both periods are very nearly the same, yielding a rake of 78° and a moment of 1.7×10^{26} dyne-cm. Figure 4 shows a comparison between the observed R1 and R2 phases and synthetics computed for the mechanism; strike N40°E, dip 54°SE, rake 78°. The method of synthesis is described by Kanamori (in preparation). The data and synthetics have been band-pass filtered to include periods from 150 to 1000 sec, and are almost indistinguishable from one another. Kristy *et al.* (1980) have also obtained a very similar focal mechanism to the one given above.

In addition to the above analysis, R1- to G1-amplitude ratios are investigated at two WWSSN stations, PRE and ARE. These stations were selected because they have clearly recorded Rayleigh and Love waves which remain on scale. R2 and G2 phases are not used because of their small amplitudes on the worldwide network. The data were digitized and band-pass filtered from 60 to 300 sec. The horizontal components were rotated into the theoretical back azimuth to give the transverse component of motion. Synthetic R1 and G1 phases were then computed using the

method, earth structure, and attenuation described by Kanamori (1970). Synthetics were passed through the same filter as the data. R1/G1 amplitude ratios are then calculated from peak-to-peak measurements. Table 2 shows the results. Much closer agreement is obtained between observed and synthetic amplitude ratios for a strike, dip, and rake of N40°E, 54°SE, and 78°, respectively, than for the mechanism obtained by considering only body-wave data. Although the above method, applied to two stations, does not have sufficient resolution to refine the mechanism further, the results do add credence to the IDA inversion solution.

Figure 5 shows an additional comparison, using the above mechanism, for R1 and R2 phases recorded on the ultralong period seismometer of the Seismographic Station of the University of California at Berkeley. The response of the Berkeley instrument is peaked at 90 sec. In each case, the data is the top, heavy trace. All waveforms have been band-pass filtered from 100 to 300 sec. The calibration of the Berkeley instrument is less well known than the calibration of the IDA instruments. For this reason, the moment estimates of 3.1×10^{26} dyne-cm and 2.0×10^{26} dyne-cm

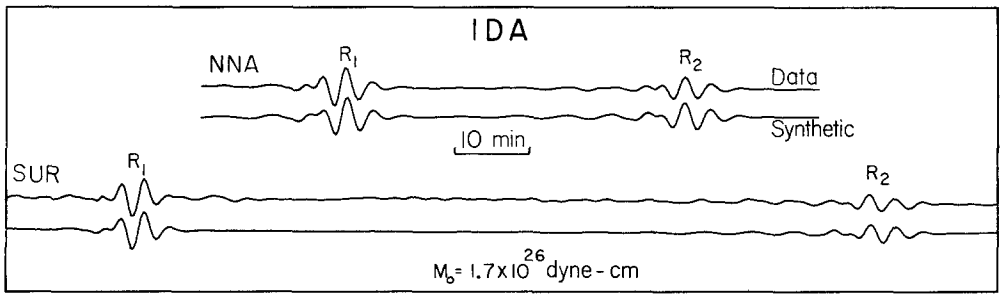

FIG. 4. Comparison between IDA data (R1 and R2) and synthetics for the mechanism; strike N40°E, dip 54°SE, and rake 78°. Both the data and synthetics are band-pass filtered from 150 to 1000 sec.

TABLE 2

R1/G1 AMPLITUDE RATIOS

Station	Data	Synthetic	
		$\theta = 40, \lambda = 78, \delta = 54$	$\theta = 40, \lambda = 47, \delta = 54$
PRE	0.88	0.71	0.34
ARE	1.17	0.82	0.25

in Figure 5 are considered less accurate than the moment of 1.7×10^{26} dyne-cm obtained from the IDA data. Also shown in Figure 5 is the theoretical Rayleigh wave radiation pattern for the preferred mechanism and a summary of the surface-wave phases used in the above analysis.

Long-period body waves (reexamined). In Figure 6, the *SH* phases have been recomputed using the new mechanism (strike N40°E, dip 54°SE, rake 78°) derived from a consideration of both body- and surface-wave data. The source depth and structure, source time function, attenuation, and number and type of rays are all the same as in Figure 3. The synthetics are very similar to those in Figure 3, except that now the more complex waveforms at ANP and HKC are fit very well. A plea to *PL*-wave contamination is no longer needed.

However, when we apply the new mechanism to *P* waves, a problem develops. The relative amplitude of direct *P* compared to later arriving energy (primarily *pP*) is too large at all stations. In Figure 7, four different source models are considered for stations VAL, COL, PRE, and HKC. These four stations are well distributed in

azimuth and exhibit typical waveshapes. All four models in Figure 7 use the same attenuation ($t^* = 1.0$) and the same fault plane solution; strike N40°E, dip 54°SE, and rake 78°. Models 1 and 2 are for a single point source at a depth of 15 km, with the same structure and source-time functions as used in Figure 2. Model 1 represents

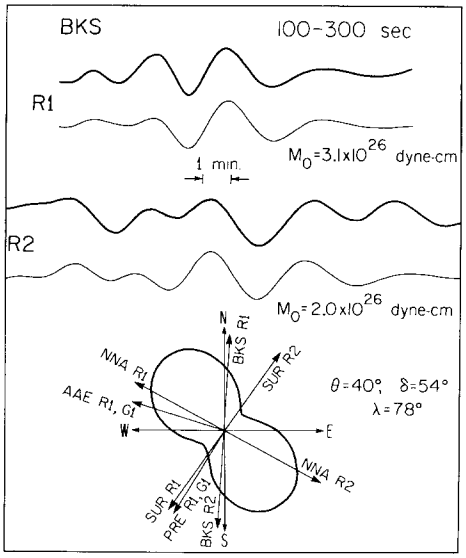

FIG. 5. Observed and synthetic Rayleigh waves (R1 and R2) for the Berkeley ultralong period instrument ($T_P = 100$, $T_g = 300$). Both the data and synthetics are band-pass filtered from 100 to 300 sec. Also shown are the theoretical Rayleigh wave radiation pattern for the preferred mechanism and the azimuths to the stations used in the surface-wave analysis.

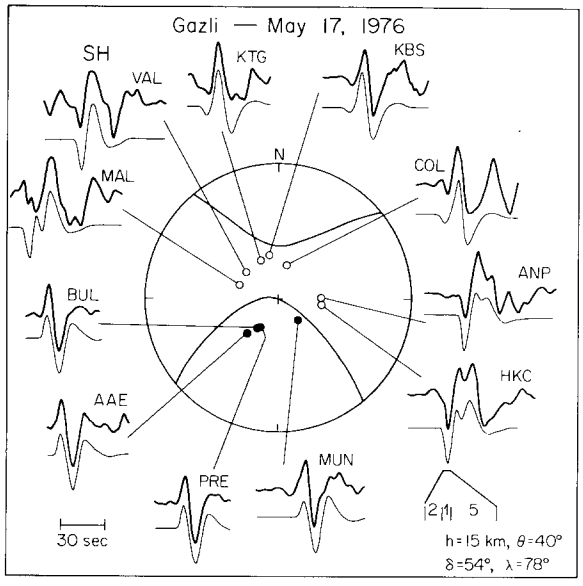

FIG. 6. Teleseismic *SH* waves for the preferred mechanism, which explains body-wave and surface-wave data. Observations are the top, heavy traces. Focal sphere is lower hemisphere projection.

the response of three rays only: direct *P*, *pP*, and *sP* from the free surface. For model 1, the amplitude of the second positive peak in the *P* waveform (predominantly *pP*) is much too small. Model 2 includes the same rays as model 1 plus *pP* and *sP* from the bottom of the sedimentary layer (layer 1, Table 1) and the three

most significant P- to SV-converted phases within the sedimentary layer. Adding these reflected and converted phases increases the amount of the later arriving energy, but the relative amplitude of direct P is still too large.

An obvious way of increasing the amplitude of pP relative to direct P is to introduce a finite source. A rupture which starts at depth and propagates up toward the surface will increase the amplitude of upgoing rays (pP, sP) compared to downgoing rays (P), through directivity (Ben-Menahem, 1961; Boore and Joyner, 1978). The above effect is caused by destructive interference in a propagating rupture, which is greatest in the direction opposite to that in which the rupture advances. Such effects have long been recognized to exist in surface-wave radiation

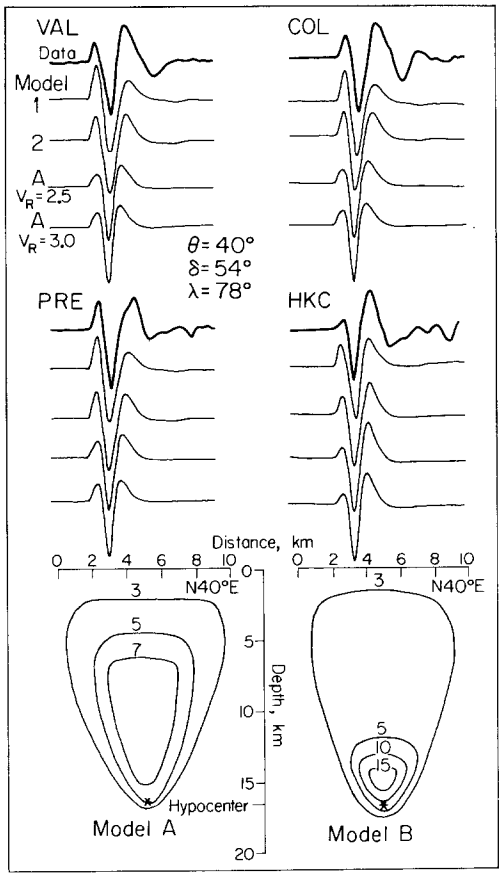

FIG. 7. Comparison between teleseismic P waves and synthetics for both point-source models (1 and 2) and finite source models (A and B).

patterns (Gutenberg, 1955) and have been proposed to explain local variations in earthquake damage (Benioff, 1955), and have also been clearly seen in laboratory models (Hartzell and Archuleta, 1979). Mikumo (1971a, b) used the azimuthal dependence of P and S waveforms to infer finite source characteristics for several deep- and intermediate-depth earthquakes. Langston (1978) used the relative amplitudes of short-period P and pP to infer that the initiation of the 1971 San Fernando earthquake rupture was bilateral, or possibly strongly unilateral downward. Thus, teleseismically observed directivity in body waves is not unknown. In addition, earthquakes are not point sources. The May 17, 1976 Gazli earthquake has

a fairly well constrained hypocenter at a depth of 15 km (primarily from short-period data). Although actual fault breakage was not observed at the surface, ground slumping and local cracking was seen (Peter Molnar, personal communication, 1979). These observations suggest that the rupture came close to the surface and that the fault plane has a minimum vertical extent of about 15 km.

The final two models in Figure 7 (labeled A) are finite-source models. A propagating rupture is approximated by taking the sum of the responses of a uniformly spaced gridwork of point sources. Figure 8 is a schematic illustration of a fault plane in a three-layer source structure. Each point source on the fault plane is given a weighting factor to approximate a uniformly varying static dislocation (diagrammatically contoured in Figure 8). The response of each point source is delayed by the time required for a circular rupture front to advance from the hypocenter, h. A similar method has been used by Hartzell *et al.* (1978) and Heaton and Helmberger (1979) to model three-dimensional finite sources. Both of the finite-fault models in Figure 7 use the same ray set as model 2 and the static dislocation values contoured at the bottom of the figure and labeled model A. The point source spacing is 500

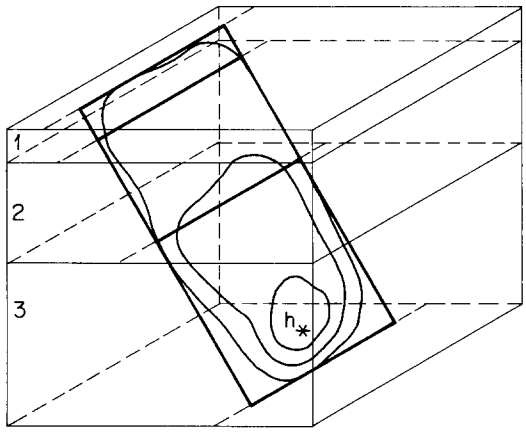

FIG. 8. Schematic illustration of finite-fault source model in a layered half-space with hypocenter at h.

meters. The contours of static dislocation are relative values. The absolute numbers are arbitrary. The rupture starts at a depth of 16.5 km and fills the area enclosed by the no. 3 contour. A basically unilateral rupture is used to maximize the desired directivity effect. The source structure is the same as given in Table 1 except that layers 2 and 3 are combined into one layer, 23.6-km thick with the material properties: $\alpha = 6.0$ km/sec, $\beta = 3.5$ km/sec, and $\rho = 2.75$ gm/cm^3. The above change has virtually no effect on teleseismic synthetics, but makes the computation simpler. N40°E has been chosen as the strike of the rupture plane. However, it should be noted that, using teleseismic data, it has not been possible to distinguish on which of the two P-wave nodal planes the rupture occurred. Choosing the other plane yields very nearly the same waveforms. Synthetics are shown for two rupture velocities, 2.5 and 3.0 km/sec. The synthetics are relatively insensitive to the rupture velocity, but there is good agreement in the P to pP amplitudes with the data.

The model A synthetics, however, predict an initial P-wave motion which is too rounded. The data show a much more pointed pulse. Several model parameter changes will sharpen the P-wave motion: (1) increasing the rupture velocity; (2)

decreasing the rupture length; (3) allowing the rupture to propagate initially bilaterally; (4) using a more spatially concentrated static dislocation distribution; or (5) a combination of the above. Alternative (1) is not favored, because a rupture velocity much greater than 3.0 km/sec is uncommon for shallow earthquakes (Geller, 1976). Alternative (2) seems even less likely, since by previous arguments, close to a minimum rupture length has already been taken. Allowing a small amount of initial downward propagation would decrease the upward directivity, but cannot be ruled out. The simplest way to produce a sharper P wave, and not adversely affect the P- to pP-amplitude ratio, is to require a more spatially concentrated static dislocation pattern. Model B at the bottom of Figure 7 is one such model. The rupture starts at a depth of 16.5 km and goes through a sharp maximum in static dislocation centered at a depth of 15 km. Such massive but localized failure is not a new concept and has been proposed for the 1971 San Fernando earthquake (Hanks, 1974), the 1975 Oroville earthquake (Hart *et al.*, 1977), and the 1975 Horse Canyon earthquake

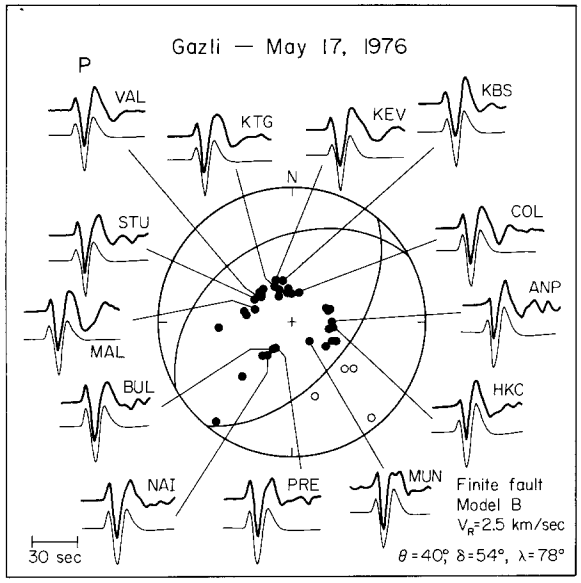

FIG. 9. Teleseismic P waves for the preferred mechanism using the finite fault model B in Figure 7. Observations are the top, heavy traces.

(Hartzell and Brune, 1979) to name a few. Figure 9 compares the model B synthetics for a rupture velocity of 2.5 km/sec with the data. Favorable agreement is obtained. The synthetics in Figure 9 have also been convolved with a trapezoidal time function with a rise of 0.1 sec, top of 0.1 sec, and fall of 3.0 sec. This convolution has a simple physical interpretation. Each point on the fault plane has a nonzero velocity for 3.2 sec. No strong significance is attached to the number 3.2, since there are trade-offs between the duration of rupture at any given point and the other faulting parameters, such as rupture velocity. However, in any physically plausible model, the above trapezoid does not shrink to a delta function. The average moment computed from P waves is 1.5×10^{26} dyne-cm, in good agreement with the moment estimated from IDA data of 1.7×10^{26} dyne-cm.

In the above analysis, efforts to explain both body-wave and surface-wave data have led to the consideration of fully three-dimensional finite sources. In the foregoing analysis, the possibility of a different focal mechanism at surface-wave

periods than at body-wave periods has been implicitly rejected. Such an interpretation seems much less likely than the one presented here. In the following section on short-period body waves, directivity effects are even more pronounced.

Short-period body waves. All available short-period, vertical WWSSN records were examined for readable *P*-wave traces. Six stations in the distance range 30° to 90° were found to have clearly recorded, digitizable traces. The records were

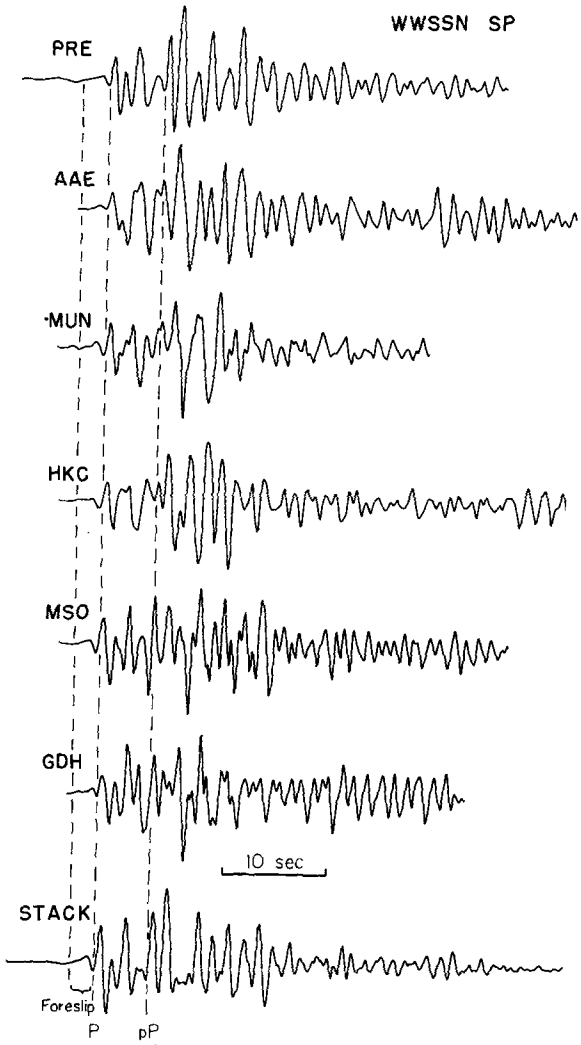

FIG. 10. Teleseismic short-period *P* waves and linear stacking of the records. The assignment of *P*- and *pP*-arrival times is based on time domain modeling.

processed in the same manner as the long-period records, except that a time step of 0.025 sec was used to preserve the high-frequency details. The six records are shown in Figure 10. There is a surprising amount of correlation between the waveforms from station to station, particularly between MSO (Missoula, Montana) and GDH (Godham, Greenland). Stations such as these may behave in a so-called transparent manner, reflecting predominantly source structure, with very little receiver structure interaction. A simple stacking of the records is shown at the bottom of Figure 10.

The stack has much the same character as each of the individual records. Each of the short-period records has an initial, low-amplitude, longer-period, compressional motion. This motion is not observable on the much lower gain, long-period records. The first arrival on the long-period records corresponds to the arrival time of the phase labeled as P in Figure 10. The leading compressional motion is interpreted as being due to precursory, low-amplitude foreslip on the fault plane. Identification of pP in Figure 10, 5.3 sec after P, is based on time domain modeling, and gives a hypocentral depth of 15 km (using the source structure in Table 1).

The study of long-period body waves in the previous sections used a crude trapezoidal approximation to the source-time function. Understanding of the short-period records requires a more detailed knowledge of the source-time function. A more accurate estimation can be obtained by simultaneous deconvolution of long- and short-period body waves (Burdick and Mellman, 1976). The above technique utilizes a broader frequency band, in which there is good signal-to-noise, by transforming both the long- and short-period records. In the cross-over band, where the responses of the long- and short-period instruments overlap, a linearly weighted sum of the two spectra is used in the deconvolution. The cross-over band used here extends from 0.125 to 0.5 Hz. Deconvolution is then used to remove the effects of attenuation ($t^* = 1.0$ for P waves) and the response of the recording instrument. To estimate the source-time function, it is necessary to isolate one particular phase. Since the hypocenter is at a depth of 15 km, the first 5.3 sec of each vertical record should be primarily direct P. Near-receiver reflected phases are assumed to be negligible within this time period. Since there exists a finite frequency band of information, the deconvolution must be limited in the frequency domain or equivalently smoothed in the time domain. Filtering is accomplished by applying the low-pass, digital, Gaussian filter with transfer function $L(f) = \exp(-f^2)$, where $f = 0.0122n$ Hz and $n = 0, 1, 2, \cdots$. $L(f) = 0.5\ L(0)$ when $f = 0.832$ Hz.

Figure 11 shows the vertical, long- and short-period records for station PRE, and their simultaneous deconvolution. At the bottom of Figure 11, the corresponding long- and short-period reconvolutions are shown (reconvolution with the attenuation operator and instrument response). The close similarity between the reconvolutions and the original records, particularly for the first 10 sec of data, serves as a check on the computations. Figure 12 shows the P-wave simultaneous deconvolution results for PRE and three other stations. Only these four stations have clearly recorded, low-noise, long- and short-period records in the distance range 30° to 90°. If the assumption that there is little receiver structure contamination in the first 5 sec is a valid one, then there is obvious strong variation in the source-time function with azimuth. The time functions in Figure 12 appear to be the sum of three or more pulses. It is tempting to relate these pulses to individual sources. Each source is then phase-delayed according to the azimuth to the station and the geometry of the rupture propagation. The different delay factors then cause the variation with azimuth of the time function. However, there is not sufficient data to say if this is the correct interpretation, and if so, what is the source distribution on the fault. But such a multiple source model is physically appealing and has been proposed for several earthquakes (Wyss and Brune, 1967; Trifunac and Brune, 1970; Müller *et al.*, 1978; Kanamori and Stewart 1978; Hartzell, 1978; to name a few).

Both single point-source and finite-source models are used to analyze the short-period records in Figure 10. The single point-source model is considered first. The structure is again the same as in Table 1, except that the top sedimentary layer is now 1.0-km thick instead of 1.4 km. A 1.0-km thick layer was found to give a slightly

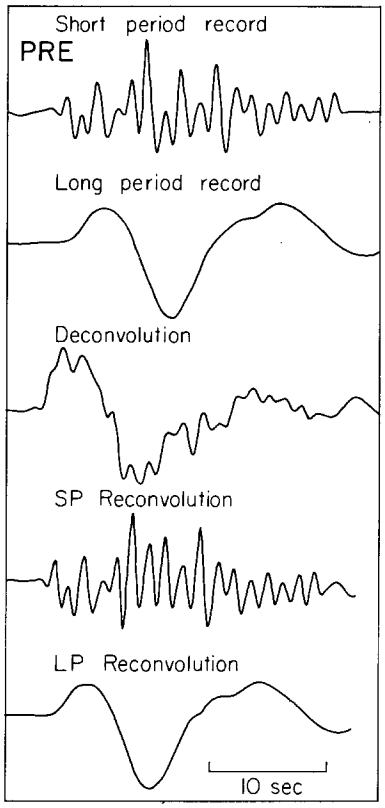

FIG. 11. Long- and short-period P waves at PRE and their simultaneous deconvolution. The deconvolution has the effects of attenuation and the recording instrument removed.

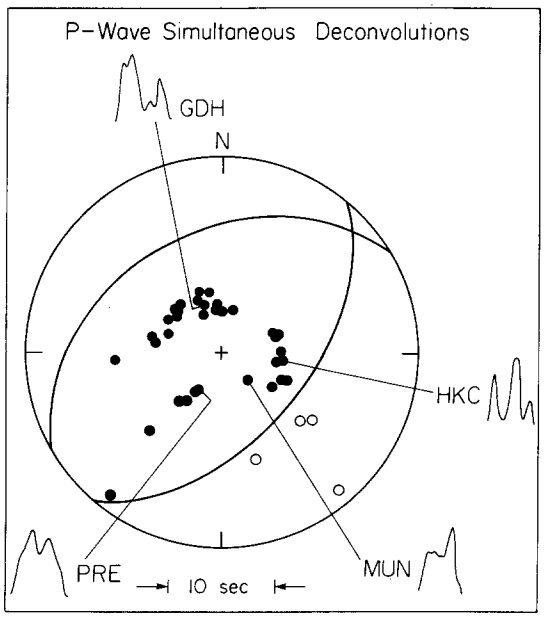

FIG. 12. Variation with azimuth of the P wave simultaneous deconvolution.

better fit to the data, however, this change is not significant. Again, the value of t^* is 1.0. Comparisons between the data and the synthetics, for a variety of source-time functions, are given in Figure 13. In each group of traces, the data is shown first, with the synthetics below. A source depth of 15 km is used. Figure 13 contrasts the difference between waveforms: (1) when the same source-time function is used for both downgoing rays (P) and upgoing rays (pP, sP); and (2) when a more spiked time function is used for upgoing rays. The source-time functions are given in the

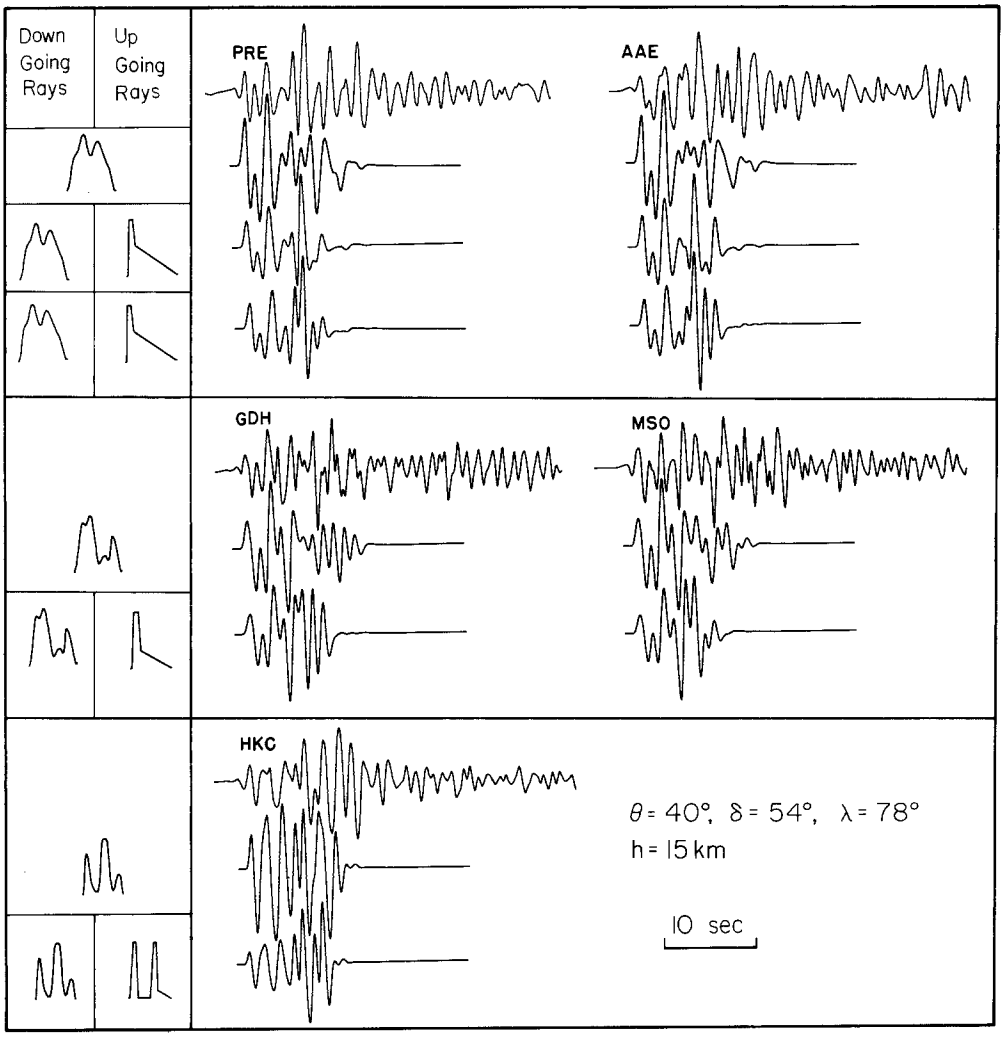

FIG. 13. Comparison of observed (top trace) and synthetic short-period teleseismic P waves for a point-source model with different source time functions. The source depth is 15 km. Different time functions are used for down-going and up-going rays to simulate a rupture propagating upward.

left-hand columns. If only one time function is shown, it is applied to both downgoing and upgoing rays. The simultaneous deconvolutions in Figure 12 are used for the time function of the downgoing ray (P) in every case. When a more spiked time function is used for upgoing rays (pP, sP), it is constructed to have the same area as the P-wave time function. It should be noted that the time functions in Figure 12 are all plotted so that they have the same peak amplitude. The more spiked time functions are intended to simulate the directivity effect of a rupture which starts at

depth and propagates toward the surface. When the P-wave time function is used for both downgoing and upgoing rays, the P-wave amplitude is much too large compared to the amplitude of pP, for each of the five stations in Figure 13. The correct amplitudes are achieved by the model which simulates an upward propagating rupture. Each of the synthetics in Figure 13 uses the same eight rays as the long-period models in Figures 2 and 9, except for the second row of synthetics for stations PRE and AAE. These two synthetics use only the three rays, direct P, pP, and sP, from the free surface. By comparing the second row of synthetics with those just beneath them, the importance of the surface sedimentary layer can be seen. The third row of synthetics adds the rays, pP and sP, from the bottom of the sedimentary layer, and the three most important P- to SV-converted phases within the sedimentary layer. These rays were also found to be important in the long-period P-wave models. They contributed to the observed P- to pP-amplitude ratios.

Although the synthetics in Figure 13 give satisfying fits to the data, the model was somewhat arbitrarily constructed. Figure 14 shows the results of a finite-fault model. A finite fault is approximated in the same manner as in Figure 9, by the summation of a gridwork of phase delayed point sources. As before, the point-source spacing is 500 meters and the structure is given in Table 1. The following values are used: $t^* = 1.0$, strike = N40°E, dip = 54°SE, and rake = 78°. Figure 14 illustrates the relative contributions of fault segments at different depths. The fault plane is divided into five contiguous subfaults, each 10-km wide and extending over a different depth range. The five subfaults, taken together, form a continuous fault plane from a depth of 0 km to a depth of 19 km. Unlike the finite-fault models at the bottom of Figure 7, all the point sources are given the same weighting factor of 1.0. The synthetics for each of the five subfaults, for stations PRE and HKC, are shown in the top half of Figure 14. Each synthetic is delayed by the time required for a circular rupture front to reach the given subfault from the hypocenter, at a depth of 15 km. The rupture velocity is 2.0 km/sec. In the bottom half of Figure 14, the synthetics for just the second and third subfaults (7.0 to 15.5 km) have been summed. The resulting synthetics are quite similar to the data. The addition of the first subfault (15.5 to 19 km) destroys this similarity. These results strongly suggest that the earthquake ruptured primarily unilaterally upward from a depth of 15 km. Also, the upper segments of the fault plane seem to contribute relatively less to the observed waveforms, at least at these periods. These results support the conclusions drawn from the analysis of the long-period body waves.

Analysis of long- and short-period body waves has put rough bounds on the dimensions of the fault plane. Waveform modeling suggests a vertical dimension of about 15 km. The horizontal extent of the fault is less well known. However, the dimension of 10 km used here is typical of fault widths for other dip-slip earthquakes of similar magnitude, such as the 1971 San Fernando earthquake (Heaton and Helmberger, 1979). For a fault area of 150 km^2, a moment of 1.6×10^{26} dyne-cm, and a rigidity, μ, of 3.0×10^{11} dyne/cm^2, the average dislocation, $\bar{u}$, is 3.3 meters. Since the rupture apparently did not reach the surface, the stress drop is estimated using the expression for a buried circular fault, $\Delta\sigma = (7\pi\mu/16)(\bar{u}/r)$ (Eshelby, 1957; Keilis-Borok, 1959), where r is the radius of the fault. The average stress drop is then 200 bars. If the faulting was more locally concentrated at depth, as the data suggest, local stress drops could have been greater than 200 bars.

Karakyr Point accelerogram. Shortly after the April 8, 1976 earthquake, the Institute of the Physics of the Earth (USSR Academy of Sciences, Moscow) installed a SSRZ three-component, optically recording accelerograph at Karakyr Point. The

location of the Karakyr Point station relative to the epicentral regions of the April 8 and May 17 events is shown in Figure 15. (Figure 15 is reproduced from Aptekman *et al.*, 1978.) Also shown in Figure 15 are other portable seismic stations, the approximate aftershock zones, and the approximate locations of fault breakage for

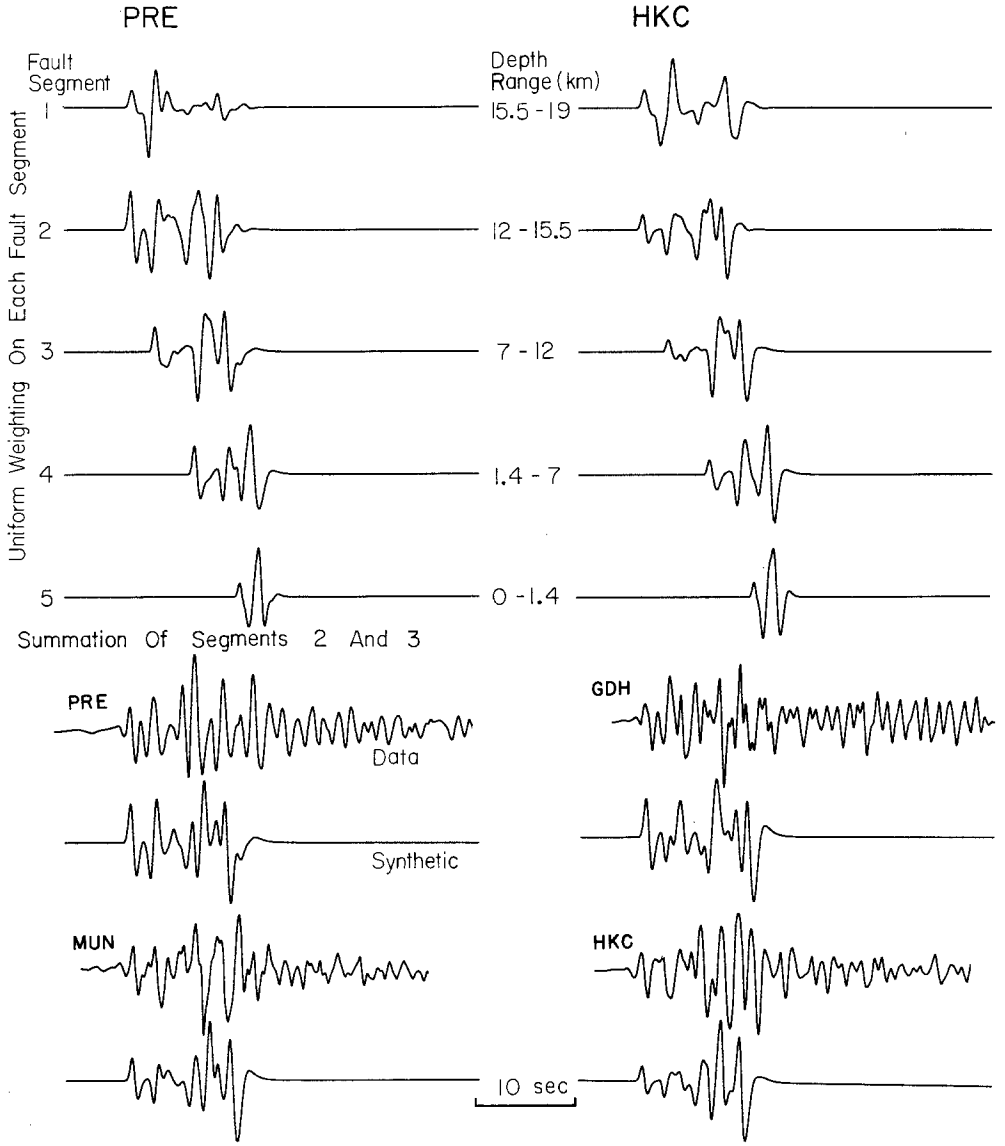

FIG. 14. Short-period synthetic *P* waves for a finite fault model, with the same mechanisms as in Figure 13. A continuous fault plane is broken up into five subfaults with different depth ranges to examine their relative contributions. The fault width is 10 km, rupture velocity is 2.0 km/sec, and hypocenter is at a depth of 15 km. Relative amplitudes for the five subfaults are (deepest fault segment first): PRE; 1.0, 0.46, 0.54, 0.91, 0.75, and HKC; 0.49, 0.60, 0.84, 1.0, 0.78.

the April 8 and May 17 earthquakes. The surface traces of fault breakage are considered to be only very approximate. Only ground slumping and accompanying local surface cracking was observed (Peter Molnar, personal communication, 1979). The Karakyr Point record is limited to the first 15 sec of motion because the film supply ran out during the earthquake. Also, a problem occurred in the film transport system. An irregular film movement took place during a 1-sec interval. The problem

was apparently corrected by the Soviets during the processing of the data, but the details are not known (Pletnev *et al.*, 1977). The Soviet digitization of the accelerograms is used in this paper. The digitization interval is 0.00657 sec.

The local magnitude, M_L, introduced by Richter (1935), is an important quantity, since of all the magnitude scales, it is determined in the period range of most relevance to engineering. The local magnitude is based on the peak amplitude recorded by a Wood-Anderson torsion seismograph with a natural period of 0.8 sec, damping constant of 0.8, and static magnification of 2800. The method of Kanamori and Jennings (1978) is used to estimate the local magnitude of the May 17 Gazli earthquake from the Karakyr Point accelerogram. Horizontal ground displacement is first calculated from the NS and EW components of acceleration. The response of a Wood-Anderson instrument is then applied to the ground motion and the local magnitude computed in the usual manner. The results are shown in Figure 16. The average M_L is 6.35. This value assumes a distance of 10 km from the fault plane to

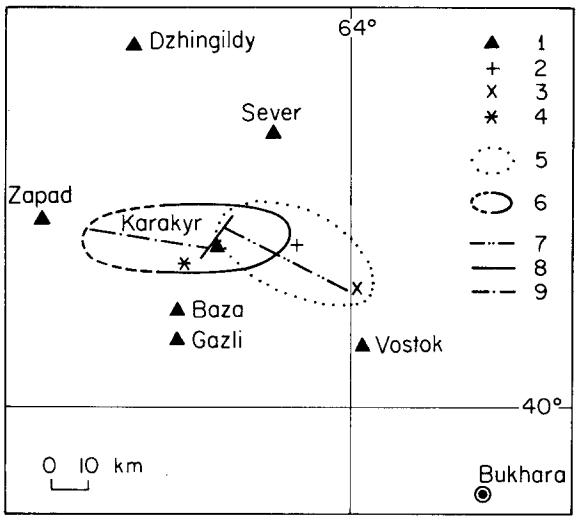

FIG. 15. Epicentral region of the April 8 and May 17, 1976 Gazli earthquakes after Aptekman *et al.* (1978). The symbols are defined as follows: 1, seismographic stations; 2, epicenter of April 8 event; 3, supposed epicentral location of large aftershock of April 8 event; 4, epicenter of May 17 event; 5, approximate location of aftershocks of April 8 event; 6, approximate location of aftershocks of May 17 event; 7, approximate location of the fault break for the April 8 event; 8, approximate location of the fault break in the initial stages of breaking for the May 17 event; and 9, approximate location of the major fault break for the May 17 event.

the station. Although the rupture started at a depth of 15 km, it did not clearly break the free surface. If surface faulting had occurred, a smaller distance of about 5 km would have been more appropriate. Values of $M_L = 6.35$ and $M_S = 7.0$ are consistent with other intraplate earthquakes (Kanamori, 1979). Lower M_L values for the same M_S value are more characteristic of interplate earthquakes, suggesting lower average stress drops for these events.

The accelerograms were integrated, baseline corrected, and high-pass Ormsby filtered, using the routines of Trifunac and Lee (1973). The Ormsby filter used has a rolloff frequency, *FN*, of 0.5 Hz and a rolloff interval, *DF*, of 0.1 Hz (Trifunac, 1971). The three components of acceleration, velocity and displacement are shown in Figure 17. Table 3 lists the corresponding peak values. The ground motion is characterized by unusually high-amplitude (1300 cm/sec^2 on the vertical), high-frequency accelerations, and low-amplitude (10 cm), low-frequency displacements. Using the station location and rough epicenter given in Figure 15, and the computed

depth of 15 km, the Karakyr Point station is then about 20 km from the hypocenter. Assuming the instrument triggered on direct P, and using the velocity structure in Table 1, the direct S wave should arrive at about 2.5 sec after the trigger time. There is an obvious corresponding arrival on both horizontal components at this time (see Figure 17). However, the largest displacements do not occur until about 6.5 sec after the trigger time, particularly on the NS and vertical components. This is roughly the arrival time one would expect for waves coming off the top of the fault, assuming a rupture length and rupture velocity of 15 km and 2.0 km/sec, respectively. However, the analysis of teleseismic body waves suggested that most of the dislocation occurred deep, below 7 km. One explanation is that the relatively

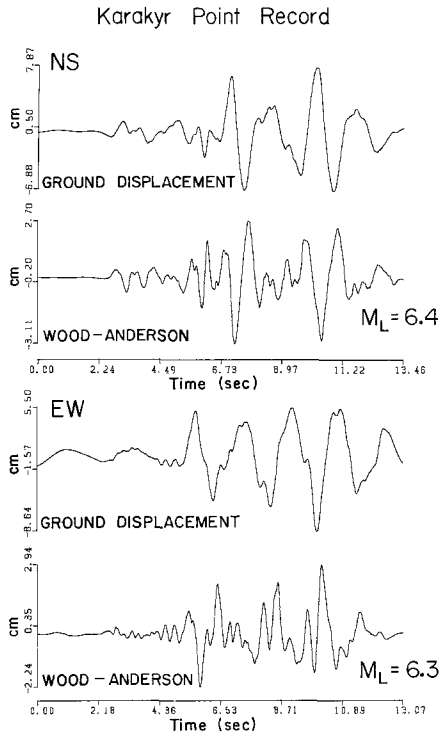

FIG. 16. Ground displacement and synthetic Wood-Anderson records computed from the Karakyr Point accelerogram.

smaller amplitude faulting in and near the surface sediments is more important, in terms of local, strong ground motion, than faulting 20 km away at depth.

Looking at the accelerations, one sees that the ground motion has decayed significantly after only about 11 sec of strong shaking. The relatively short duration of strong shaking supports the previous conclusion that the rupture propagated primarily upward and thus toward the station. Propagation toward the station compresses the effective rupture time. The large-amplitude, high-frequency accelerations, which are particularly dramatic on the vertical component, may be due in part to the focusing effect of the propagating rupture. High-frequency resonances, caused by the faulting of the surface sediments, may also play an important role. Unfortunately, the location of the station relative to the fault plane (Figure 15) is known only very generally, at best. For this reason, attempts to model the strong

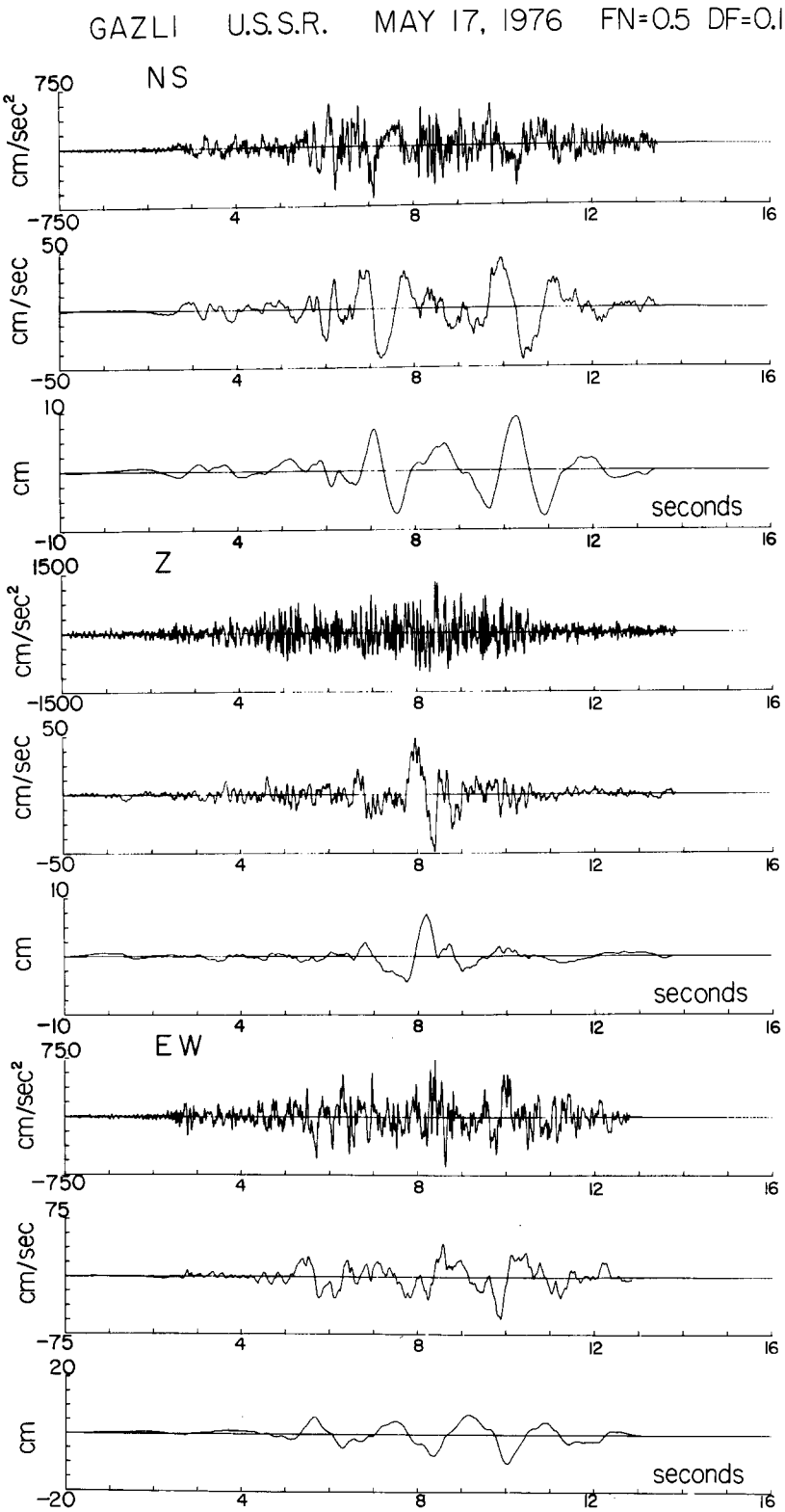

FIG. 17. Accelerations, velocities, and displacements from the Karakyr Point accelerograph.

ground motion with a finite-source model have been hindered and have been delayed until better location information is available.

Discussion

From the study of the May 17, 1976 Gazli earthquake, several points of general importance can be mentioned. We have seen that it is possible, particularly for dip-slip earthquakes, to obtain a fault plane solution which does a reasonably good job of explaining body waveforms (both *P* and *SH*), but is still not well constrained. This problem arises because one is always working with a limited amount of data. Unless the stations are sufficiently numerous, and advantageously distributed, it is very difficult to pin down both nodal planes. Surface-wave data can then be helpful in constraining the mechanism.

Directivity effects due to a propagating rupture are apparent in the teleseismic *P* waveforms of the May 17 earthquake. These effects are most likely intensified by a unilateral rupture, which started at a depth of 15 km and ruptured almost to the surface. For such an earthquake, one should properly use a finite-source model. The *SH* waveforms have also been calculated using finite-fault models, but the results are less definitive than for the *P* waves. This observation is attributed to the difficulty in obtaining accurate, uncontaminated, rotated *SH* phases at a wide range of azimuths. The overall faulting can be characterized as progressing from bottom to top. But on a somewhat more detailed scale, the data suggests that the rupture initiated with localized, massive failure, and then slowly died out as it made its way

TABLE 3

Peak Values for Karakyr Point Record

	EW	NS	Z
Acceleration (cm/sec^2)	738.0	656.0	1300.0
Velocity (cm/sec)	54.0	44.0	49.0
Displacement (cm)	10.0	9.0	7.1

toward the surface. There is a degree of interpretation in the above model, but faulting involving localized failure, or asperities, or barriers is a recurring theme in the literature. Similar models have been proposed to explain both large and small earthquakes alike. If one looks at finer detail, with the results of simultaneous deconvolution of long- and short-period records, the picture becomes more complicated. Estimation of the source-time function by the above method suggests possible multiple asperities or sources. Of course, this result must be tempered with the fact that every earthquake source can probably be interpreted in terms of multiple sources, depending on how high a frequency one is willing to consider.

The thick sediments in the source region (~1 km) have an important effect on both the teleseismic records and the local, strong ground motion. *pP*, *sP*, and *sS* reflected from the base of the sedimentary pile, as well as *P*- to *SV*-converted phases within the sediments, are all significant teleseismic phases for the Gazli earthquakes. Although the analysis of the strong ground motion records is not complete, the sediments probably contributed to the high-frequency ringing in the acceleration records. Finally, the overall duration, and prominent arrivals seen in the strong ground motion are consistent with the general aspects of the faulting process deduced from the analysis of the teleseismic records.

Acknowledgments

The author benefited greatly from discussions with Donald Helmberger, Tom Heaton, Gordon Stewart, and John Ebel. Computer programs were used which were written in part or totally by Donald

Helmberger, Tom Heaton, Hiroo Kanamori, and Larry Burdick. Gordon Stewart assisted greatly with the surface-wave analysis, as did Tom Heaton with the body-wave analysis. This research was supported by the Earth Sciences Section, Natonal Science Foundation Grant PFR 7808813 and by the Advanced Research Projects Agency of the Department of Defense and was monitored by the Air Force Office of Scientific Research under Contract F49620-77-C-0022.

REFERENCES

Agnew, D., J. Berger, R. Buland, W. Farrell, and F. Gilbert (1976). International deployment of accelerometers: a network for very long period seismology, *EOS, Trans. Am. Geophys. Union* **57,** 180–188.

Aptekman, kh.Ya, V. M. Graizer, K. G. Pletnev, D. N. Rustanovich, N. V. Shebalin, and V. V. Shteinberg (1978). Some data on processes in the epicentral zone of the 1976 Gazli earthquakes, in *Epicentral Zones of Earthquakes, 19,* Questions in engineering seismology, Nauka, Moscow, 149–166 (in Russian).

Benioff, H. (1955). Mechanism and strain characteristics of the White Wolf fault as indicated by the aftershock sequence, in *Earthquakes in Kern County, California during 1952,* G. B. Oakeshott, Editor, *Calif. Div. Mines Bull.* **171,** 199–202.

Ben-Menahem, A. (1961). Radiation of seismic surface waves from finite moving sources, *Bull. Seism. Soc. Am.* **51,** 401–435.

Boore, D. M. and W. B. Joyner (1978). The influence of rupture incoherence on seismic directivity, *Bull. Seism. Soc. Am.* **68,** 283–300.

Burdick, L. J. and G. R. Mellman (1976). Inversion of the body waves from the Borrego Mountain earthquake to the source mechanism, *Bull. Seism. Soc. Am.* **66,** 1485–1499.

Carpenter, E. W. (1966). Absorption of elastic waves—An operator for a constant Q mechanism, *Atomic Weapons Res.* Estab. Rep. 0-43/66, Her Majesty's Sta. Office, London.

Davydova, N. I., Yu. F. Ivanstov, B. B. Tal'-Virskii, A. N. Fursov, and G. A. Yaroshevskaya (1975). Properties of deep-seated seismic boundaries in western Uzbekistan, in *Seismic Properties of the Mohorovičić Discontinuity,* N. I. Davydova, Editor, Jerusalem.

Ebel, J. (1979). Fault roughness as inferred from the teleseismic short period P waves and strong motion recordings of the Borrego Mountain earthquake (abstract), *EOS, Trans. Am. Geophys. Union* **60,** 896.

Eshelby, J. D. (1957). The determination of the elastic field of an ellipsoidal inclusion and related problems, *Proc. Roy. Soc. London, Ser. A,* **241,** 376–396.

Futterman, W. I. (1962). Dispersive body waves, *J. Geophys. Res.* **67,** 5279–5291.

Geller, R. J. (1976). Scaling relations for earthquake source parameters and magnitudes, *Bull. Seism. Soc. Am.* **66,** 1501–1523.

Gutenberg, B. (1955). Magnitude determination for larger Kern County shocks, 1952; effects of station azimuth and calculation method, in *Earthquakes in Kern County, California during 1952,* G. B. Oakeshott, Editor, *Calif. Div. Mines Bull.* **171,** 171–175.

Hanks, T. C. (1974). The faulting mechanism of the San Fernando earthquake, *J. Geophys. Res.* **79,** 1215–1229.

Hart, R. S., R. Butler, and H. Kanamori (1977). Surface-wave constraints on the August 1, 1975, Oroville earthquake, *Bull. Seism. Soc. Am.* **67,** 1–7.

Hartzell, S. H. (1978). Earthquake aftershocks as Green's functions, *Geophys. Res. Letters* **5,** 1–4.

Hartzell, S. H., G. A. Frazier, and J. N. Brune (1978). Earthquake modeling in a homogeneous half-space, *Bull. Seism. Soc. Am.* **68,** 301–316.

Hartzell, S. H. and R. J. Archuleta (1979). Rupture propagation and focusing of energy in a foam rubber model of a stick slip earthquake, *J. Geophys. Res.* **84,** 3623–3636.

Hartzell, S. H. and J. N. Brune (1979). The Horse Canyon earthquake of August 2, 1975—Two-stage stress-release process in a strike-slip earthquake, *Bull. Seism. Soc. Am.* **69,** 1161–1173.

Heaton, T. H. and D. V. Helmberger (1979). Generalized ray models of the San Fernando earthquake, *Bull. Seism. Soc. Am.* **69,** 1311–1341.

Helmberger, D. V. (1974). Generalized ray theory for shear dislocations, *Bull. Seism. Soc. Am.* **64,** 45–64.

Kanamori, H. (1970). Synthesis of long-period surface waves and its application to earthquake source studies—Kurik Islands earthquake of October 13, 1963, *J. Geophys. Res.* **75,** 5011–5027.

Kanamori, H. (1979). A semi-empirical approach to prediction of long-period ground motions from great earthquakes, *Bull. Seism. Soc. Am.* **69,** 1645–1670.

Kanamori, H. and P. C. Jennings (1978). Determination of local magnitude M_L, from strong-motion accelerograms, *Bull. Seism. Soc. Am.* **68,** 471–485.

Kanamori, H. and G. S. Stewart (1978). Seismological aspects of the Guatemala earthquake of February 4, 1976, *J. Geophys. Res.* **83,** 3427–3434.

Keilis-Borok, V. (1959). On estimation of the displacement in an earthquake source and of source dimensions, *Ann. Geofis.* (Rome) **12,** 205–214.

Kostrov, B. V. (1964). Self-similar problems of propagation of shear cracks, *J. Appl. Math. Mech.* **28,** 1077–1087.

Kristy, M. J., L. J. Burdick, and D. W. Simpson (1980). The focal mechanisms of the Gazli, USSR earthquakes (submitted for publication).

Langston, C. A. (1978). The February 9, 1971 San Fernando earthquake: a study of source finiteness in teleseismic body waves, *Bull. Seism. Soc. Am.* **68,** 1–29.

Langston, C. A. and D. V. Helmberger (1975). A procedure for modeling shallow dislocation sources, *J. Geophys.* **42,** 117–130.

Mikumo, T. (1971a). Source process of deep and intermediate earthquakes as inferred from long-period P and S waveforms 1. Intermediate-depth earthquakes in the southwest Pacific region, *J. Phys. Earth* **19,** 1–19.

Mikumo, T. (1971b). Source process of deep and intermediate earthquakes as inferred from long-period P and S waveforms 2. Deep-focus and intermediate-depth earthquakes around Japan, *J. Phys. Earth* **19,** 303–320.

Müller, G., K. P. Bonjer, H. Stöckl, and D. Enescu (1978). The Romanian earthquake of March 4, 1977: I. Rupture process inferred from fault-plane solution and multiple-event analysis, *J. Geophys.* **44,** 203–218.

Pletnev, K. G., N. V. Shebalin, and V. V. Shteinberg (1977). Strong-motion records from the May 1976 Gazli USSR earthquakes, *U.S. Geol. Surv., Circular 762-A,* 3–5.

Richter, C. F. (1935). An instrumental earthquake scale, *Bull. Seism. Soc. Am.* **25,** 1–32.

Trifunac, M. D. and J. N. Brune (1970). Complexity of energy release during the Imperial Valley, California, earthquake of 1940, *Bull. Seism. Soc. Am.* **60,** 137–160.

Trifunac, M. D. (1971). Zero baseline correction of strong-motion accelerograms, *Bull. Seism. Soc. Am.* **61,** 1201–1211.

Trifunac, M. D. and V. Lee (1973). Routine computer processing of strong-motion accelerograms, *Earthquake Eng. Res. Lab. Rept.* EERL 73-03, California Institute of Technology, Pasadena.

Wyss, M. and J. N. Brune (1967). The Alaska earthquake of 28 March 1964: a complex multiple rupture, *Bull. Seism. Soc. Am.* **57,** 1017–1023.

SEISMOLOGICAL LABORATORY
CALIFORNIA INSTITUTE OF TECHNOLOGY
PASADENA, CALIFORNIA 91125
CONTRIBUTION NO. 3423

Manuscript received March 17, 1980